Research Square

Preprints are preliminary reports that have not undergone peer review. They should not be considered conclusive, used to inform clinical practice, or referenced by the media as validated information.

A single-wire, large-area, super-resolution electromagnetic skin enabling human-level spatial acuity

Arindam Basu

arinbasu@cityu.edu.hk

City University of Hong Kong https://orcid.org/0000-0003-1035-8770

Gaishan Li

City University of Hong Kong

Jiachen Du

City University of Hong Kong

Yiqing Sun

City University of Hong Kong https://orcid.org/0000-0001-8562-0599

Shuai Dong

City University of Hong Kong

Chiara Bartolozzi

Istituto Italiano di Tecnologia https://orcid.org/0000-0003-3465-6449

Geng-Bo Wu

City University of Hong Kong https://orcid.org/0000-0002-8226-1663

Article

Keywords:

Posted Date: October 22nd, 2026

DOI: https://doi.org/10.21203/rs.3.rs-10823611/v1

License: This work is licensed under a Creative Commons Attribution 4.0 International License. Read Full License

Additional Declarations: There is **NO** Competing Interest.

A single-wire, large-area, super-resolution electromagnetic skin enabling human-level spatial acuity

Gaishan Li[1,*], Jiachen Du[1,4,*], Yiqing Sun[1], Shuai Dong[1], Chiara Bartolozzi[2], Geng-Bo Wu[1,5+], and Arindam Basu[1,5+]

[1]Department of Electrical Engineering, City University of Hong Kong, Hong Kong SAR, China.
[*]Equal Contribution
[+]Correspondence to arinbasu@cityu.edu.hk and bogwu2@cityu.edu.hk
[2]Italian Institute of Technology, Genoa, Italy.
[4]Pengcheng Laboratory, Shenzhen, China.
[5]State Key Laboratory of Terahertz and Millimeter Waves, City University of Hong Kong, Hong Kong SAR, China.

ABSTRACT

Large area tactile sensing is widely needed in human machine interfaces, prosthetics and for collaborative robots. However, scaling tactile sensing to larger areas or to higher spatial resolution typically involves a direct tradeoff with the number of sensing units, wiring complexity, and fabrication cost. Inspired by the properties of human skin, super-resolution (SR) sensing has reduced the number of required sensors, but simultaneously achieving large area coverage with high spatial resolution, measured by the SR factor, remains unresolved. Here, we present a new SR method using a 2D meandering spoof surface plasmon polariton (SSPP) transmission line that solves all the challenges above. Combining principles of frequency-diverse computational sensing with deep neural networks, the proposed electromagnetic skin uses a single wire to achieve SR factors exceeding $10,000$, an order of magnitude more than other approaches, while covering sensing areas of $2500-28,800$ mm^2. The EM-skin facilitates human computer interaction with dynamic tactile stimulus and object recognition with high accuracies. Overall, this work provides a promising route towards highly scalable large-area e-skin with super-resolution sensing.

Main

Tactile sensing is indispensable for a broad range of robotic applications, providing a critical information channel for robot–environment interaction beyond vision[1–5]. Consequently, a wide variety of tactile sensing technologies have been developed, including resistive[1,6–9], capacitive[10–12], piezoelectric[13], vision-based[14,15], triboelectric[16,17], and magnetic[18–21] approaches. The fundamental sensing unit in these systems is commonly referred to as a taxel. However, achieving human-skin-like tactile perception—namely, simultaneously realizing high spatial resolution and large-area coverage—remains a longstanding challenge[22–24]. Covering whole body of humanoid robots becomes especially important for collaborative robots that share workspaces with humans[25]. Increasing spatial resolution generally requires integrating a larger number of smaller taxels and routing dedicated interconnects for signal readout[7], while expanding the sensing area similarly necessitates additional sensing units. The resulting escalation in wiring complexity, fabrication difficulty, and system cost makes it impractical to attain human-skin-level tactile perception simply by densely tiling large surfaces with taxels[24].

A promising solution can be inspired by the operating principles of human skin, which is capable of resolving spatial details beyond the physical spacing of mechanoreceptors[26–29]. This capability of super resolution (SR) arises from the overlapping receptive fields of mechanoreceptors (Fig. 1**b**): an external stimulus simultaneously activates multiple receptors, and the nervous system integrates these distributed responses to infer stimulus location with substantially enhanced precision[28,29]. Inspired by this principle, various SR tactile sensing strategies have been proposed (Extended Data Table 1), where the SR factor is a combined metric used to quantify the tradeoff between localization, area coverage and number of sensors. Compared to conventional crossbar-based resistive, capacitive, and piezoresistive architectures, SR tactile sensors can often achieve large-area tactile sensing with significantly fewer physical taxels[30–32]. Alternatively, vision-based tactile sensors[14,33] can provide exceptionally high resolution owing to the large pixel counts of modern cameras, although their geometries and integration schemes are often structurally constrained. Fibre-Bragg-grating-based photonic tactile sensors[4] offer greater structural flexibility, but typically exhibit lower localization accuracy. Another approach using specialized magnetic films and Hall-effect sensors can simultaneously achieve high accuracy and relatively large SR factors, albeit at the expense of increased fabrication complexity[19,32]. Overall, high localization accuracy, mechanical flexibility, and fabrication simplicity

remain difficult to attain simultaneously.

In this article, to overcome the above challenges (Fig. 1**a,c**), we present electromagnetic skin (EM-skin)–an original tactile sensing modality that intrinsically supports SR for large area skin, based on the detection of electromagnetic field distortions caused by physical contact. The system is based on electromagnetic surface waves combined with artificial intelligence algorithms. Spoof surface plasmon polaritons (SSPP) translate optical surface plasmons to the microwave and terahertz regimes through subwavelength metallic corrugations, supporting strong electromagnetic field confinement and low-loss propagation[34,35] with tunable dispersion[36,37]. This strong field confinement makes the propagation of an SSPP highly sensitive to local perturbations of its electromagnetic environment - a property that we leverage to detect and localize perturbations due to externally applied pressure. By routing an SSPP transmission line across a two-dimensional sensing surface and sweeping the excitation frequency from both ends, spatially diverse electromagnetic field distributions are generated that encode object position into frequency-dependent scattering parameters (Fig. 1**c-e**). In this framework, the port at each end functions as a virtual sensor. To solve the resulting inverse problem of finding object location from scattering parameters, a multi-branch multilayer perceptron (MLP) is trained to exploit the complementary information contained in the dual-port spectral responses[38], thereby mapping high-dimensional frequency-domain features to spatial coordinates (Fig. 1**e**). Because spatial information is encoded entirely in the dual-port spectral response of a single transmission line, enlarging the sensing area requires neither additional physical taxels nor increased wiring complexity, endowing the architecture with intrinsic scalability. We validated this using two prototype EM-skins varying by an order of magnitude from 5×5 to 16×18 cm^2 (Fig. 1**f**), both of which displayed SR factors exceeding $10,000$, that is more than ≈ 12 times higher than any other state-of-the-art approach. In addition, the system attains 91% classification accuracy in identifying eight common everyday objects, establishing a new paradigm for tactile sensing and provides a promising route towards scalable, large-area, and high-precision electronic skin systems used for robotics, prosthetics and human-machine interfaces such as touchpads.

Results

Principle of electromagnetic skin (EM-skin)

Frequency-diverse computational sensing exploits frequency-dependent field patterns to collect the scattering information of unknown objects[39–45]. Inspired by frequency-diverse computational sensing, a high-precision EM-skin system is designed using an SSPP transmission line implemented on a flexible substrate (Fig. 1**c**). Rather than tiling the sensing plane with a large number of discrete sensing units, plane-wide sensing is achieved by injecting electromagnetic waves from two ports and leveraging their spatially distributed fields to sensing the entire surface. Due to the continuous wave propagation in the SSPP, enlarging the sensing area does not inherently require more sensors[7,16]. Combined with low-cost materials, a simple fabrication workflow, and millimetre-scale localization error, the sensing platform is naturally scalable in sensing area. In contrast to other Hall-sensor-based magnetic skins[19,32], which typically require Hall sensors to be integrated on a PCB, the proposed sensor is fully flexible and can conform to a wide range of curved surfaces.

Specifically, frequency-swept waves from 7 to 13 GHz are injected into Port 1 and Port 2, respectively. The resulting fields are not confined to the copper-covered region; instead, they extend across the entire 2D sensing plane and into the surrounding space several millimetres above it. As illustrated in Fig. 1**d**, when an object enters the field region, waves at different frequencies produce distinct scattering parameters (S-parameters) depending on the object's shape, position, and material properties. As shown in Fig. 1**a**, when the probe is placed at different positions on the 2D sensing plane, the measured S-parameters (S_{11} and S_{22}) exhibit clear and structured spatial intensity patterns. In the vicinity of Port 1 (Port 2), S_{11} (S_{22}) becomes significantly stronger. Each port can therefore be regarded as an individual sensor, with its sensitive area defined by the region where the S-parameter response is pronounced; the overall sensing plane is given by the union of the sensitive areas of the two ports. This design philosophy is aligned with super-resolution e-skin concepts[19,30–33,46–48], which emulate biological tactile perception by creating overlapping sensing fields and inferring tactile information from differential responses, thereby forming virtual taxels.

To localize objects across the full plane, the one-dimensional transmission line is routed through an engineered meandering topology that maps its propagation coordinate onto known positions in the sensing plane. Objects within the near-field region perturb nearby line segments through evanescent coupling, so that the measured reflection spectrum can be modelled as a geometry-weighted projection of the two-dimensional perturbation distribution onto the routed propagation path. Discretizing the sensing plane into N cells, the reflection coefficient at each frequency ω_ℓ is well approximated by a linear combination of the local perturbations,

$$\Gamma \simeq \mathbf{K}\mathbf{q}, \tag{1}$$

where Γ is the measured response vector, $\mathbf{q} = (q_1, \ldots, q_N)^{\mathrm{T}}$ contains the perturbation strengths in the discretized cells, and the sensing matrix $\mathbf{K}$ encodes the routed-line geometry. Resolving the line into M segments, each kernel element combines the evanescent coupling between cell p and every segment m with the round-trip phase accumulated along the propagation

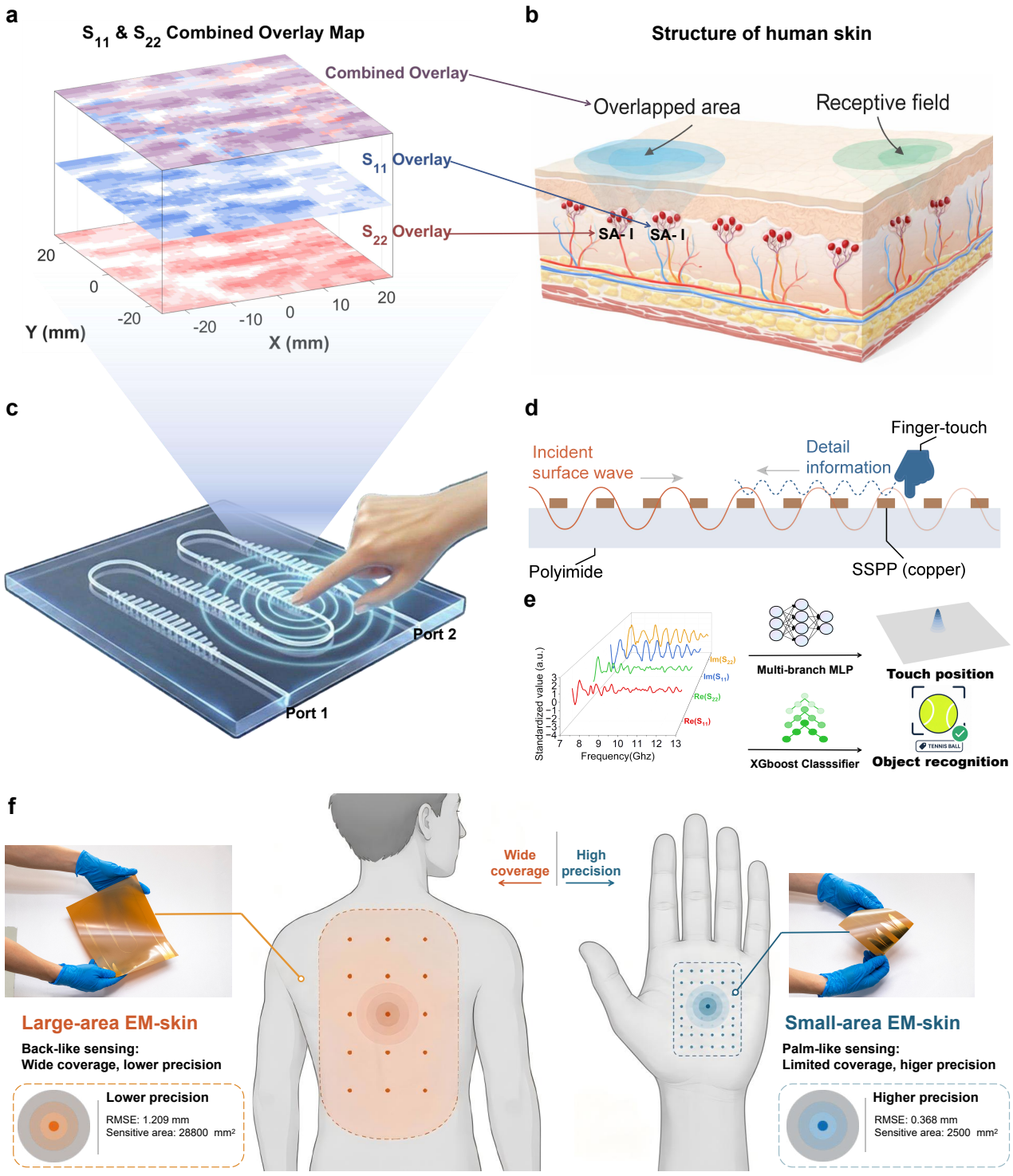

Fig. 1. Overview and working principle of electromagnetic skin (EM-skin). a The highlighted regions indicate the signal-intensity distributions of the reflection coefficients S_{11} and S_{22} as the object is placed at different locations on the EM-skin shown in (c). **b** SA-I type mechanoreceptors in the human body have a mechanism for coordinated operation by overlapping their receptive fields. By interpreting information from different mechanoreceptors, the human body possesses excellent contact localization capabilities and serves as inspiration for our work. (Modified using AI tools from source[30]) **c** The EM-skin uses a 2D transmission line in SSPP structure. (Enhanced using AI tool) **d** The electromagnetic field of the SSPP transmission line extends throughout the surrounding three-dimensional space. When a finger is placed within the field, it induces a reflected wave. **e** The measured reflected signals from the two ports provide multi-spectral features. The four channels correspond to the real and imaginary components of S_{11} and S_{22}. Feeding these high-dimensional features into a trained neural network enables high-precision localization. **f** The EM-skin system proposed in this paper can seamlessly handle large-area sensing across multiple scales, with proportional scaling of resolution, as done in the human body by varying mechanoreceptor density. (Parts of this figure were enhanced using AI tool)

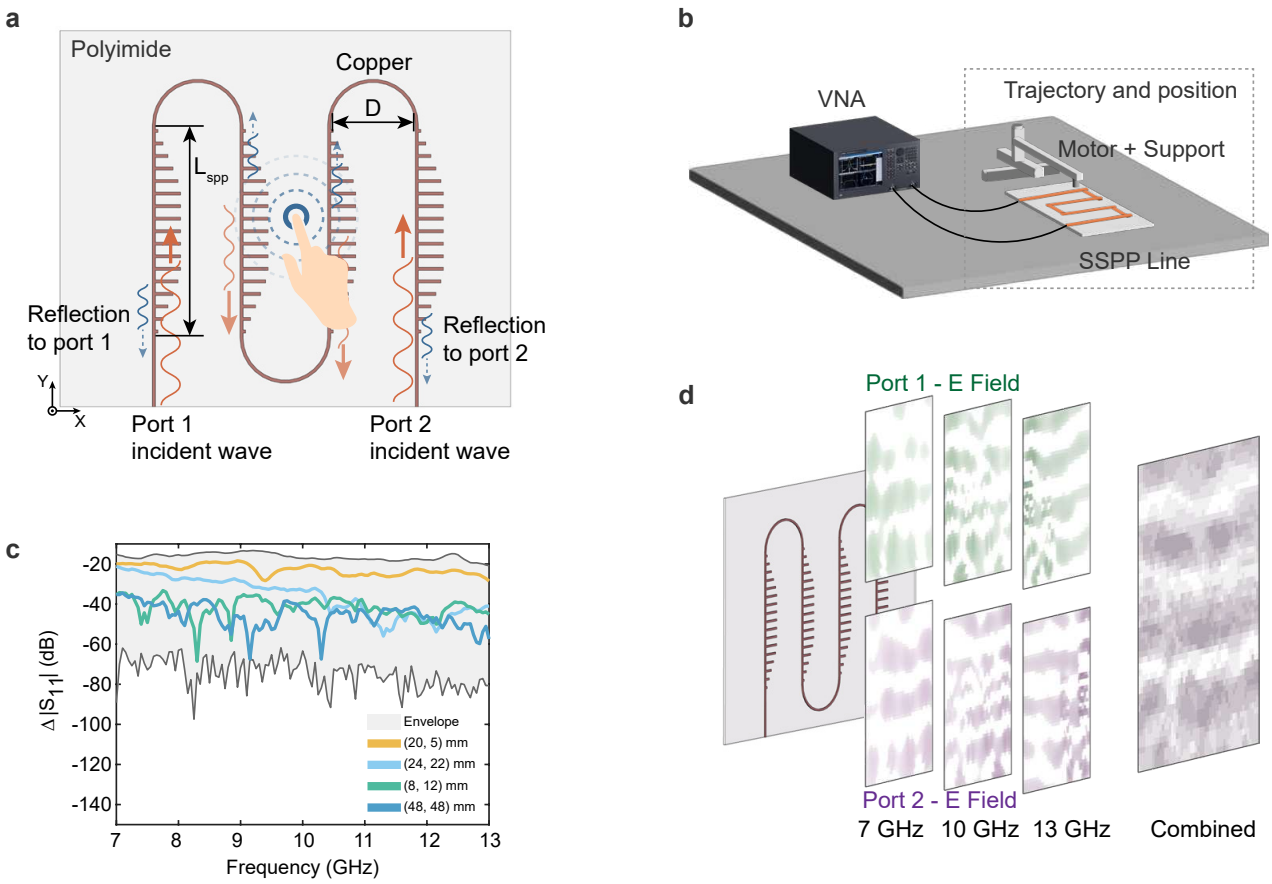

Fig. 2. Transmission line sensing theory and system configuration. a The schematic of the proposed two-dimensional SSPP transmission line sensing hardware showing the main parameters of the physical structure: length of the SSPP branch L_{spp} and inter-branch distance D. **b** The test setup for trajectory and position sensing. A motorized mechanical support is used to move the object precisely and place it in multiple locations on the EM-skin. **c** The variation of S_{11} when an object is placed at different positions in the sensing plane confirm the ability to sense location based on spectral information. The gray area represents the range of all ΔS_{11} data. **d** The use of electric fields at different frequencies and two ports establishes full coverage of the EM-skin across locations.

coordinate,

$$K_{\ell p} = \Delta A_p \sum_{m=1}^{M} \exp\left[-\alpha\sqrt{(x_p - X_m)^2 + (y_p - Y_m)^2}\right] \exp[-2j\beta(\omega_\ell)\, s_m]\, \Delta s_m, \tag{2}$$

where (x_p, y_p) and (X_m, Y_m) are the positions of cell p and segment m, s_m and Δs_m are the propagation coordinate and length of segment m, ΔA_p is the area of cell p, α is the transverse evanescent decay constant, and $\beta(\omega_\ell)$ is the propagation constant(see Methods for detailed derivation). The distance-dependent term sets the near-field coupling strength, whereas the phase term encodes the position of each segment along the line, so that objects at distinct locations produce distinguishable spectral signatures. Localization is thus posed as an inverse problem, in which the object position is recovered by inverting Eq. 1 to find the spatial response that best explains the measured reflection.

We validated this approach on a 50 mm × 50 mm flexible EM-skin prototype fabricated on a polyimide (PI) substrate, using a vector network analyzer (VNA) to measure the broadband reflection responses from both ports (Fig. 2b; details in Methods). Consistent with Eq. 1, the perturbation amplitude depends strongly on position (Fig. 2c). Locations near the transmission line produce larger variations in ΔS, while regions between line segments produce weaker responses. At a single frequency, however, different positions can produce similar reflection changes, because the measurement provides only a limited projection of the two-dimensional perturbation field. We therefore exploit frequency diversity through broadband measurement, generating a set of frequency-dependent response maps (Fig. 2d) that improve the separability of pixels within the sensing area. Dual-port reflection measurements further mitigate attenuation along the propagation path, because S_{11} and S_{22} emphasize perturbations closer to opposite ends of the routed line and together improve the uniformity of sensitivity across the plane.

Scalability and Localization Accuracy

Having established a general theoretical and computational framework for localization, we next examined whether the SSPP-based sensing architecture could be extended across device scales and geometric layouts without losing its localization capability. Specifically, we tested whether the surrogate kernel, $\mathbf{K}(\omega)$, derived from the theoretical model remained valid when implemented in physically distinct transmission-line structures. To this end, we fabricated a larger flexible SSPP transmission-line prototype (Fig. 3a), differing by more than an order of magnitude in sensing area. The larger SSPP prototype operates at a lower frequency range of 4 to 10 GHz to minimize transmission line propagation losses. We first evaluated this scalability numerically by calculating the mean absolute error (MAE) under different SSPP-line lengths L_{spp} and interline gaps D (Fig. 3b). The detailed experimental details are in Section Supplementary Note S4. As expected from the near-field exponential decay described by Eq. 2, increasing the interline gap weakened the target-induced perturbation coupled into the SSPP line. Consequently, the MAE increased with both D and L_{spp}. However, this increase was gradual and remained moderate in relation to the expansion of the sensing region, suggesting that the proposed SSPP transmission-line architecture can be scaled to larger sensing areas while retaining sufficient field sensitivity for spatial localization.

These findings were then experimentally validated on both protoypes (see Methods for dataset acquisition) by training a multi-branch neural network for position estimation (Fig. 3c) on the spectral encodings. The complex differential spectra, ΔS_{11} and ΔS_{22}, were decomposed into real and imaginary components, which were provided to four independent input branches. Features extracted from these branches were concatenated in a fusion layer and passed to a multilayer perceptron (MLP) that approximated the inverse mapping to estimate the object coordinates. Experimental results (Fig. 3d–f) validated this theory, with the localization errors increasing proportional to the size, implying similar relative errors for both prototypes. The corresponding root-mean-square error (RMSE) maps showed no pronounced degradation across most of the sensing domain, and the cumulative distribution function (CDF) profiles confirmed that the localization error remained below one-third of the calibration pitch for the majority of test positions. These results demonstrate stable sub-pixel localization across substantially different device sizes, confirming that our approach generalizes across different sizes and geometries. As shown in Fig. 3g, compared with state-of-the-art works, our approach achieves the highest SR factor with a relatively large sensing area.

Dynamic sensing for Human Machine Interface

Next, we demonstrated the suitability of the EM-skin as a touchpad with dynamic tactile stimuli (Fig. 4**a**). Using the measured reflection coefficient, the trained neural network was able to correctly trace (by continuously localizing over time the tip of the robot finger) alphabets written by the robotic arm (Fig. 4**b** and Supplementary Video 1) in real time. To further evaluate the capability of the EM-skin system in capturing more intricate trajectories, ten distinct trajectories were generated (by moving the robot arm at ≈ 1 Hz) for digits $0-9$, similar to the MNIST dataset[49]. Examples of the reconstructed handwritten digits are shown in Fig. 4**c**. Using a convolutional neural network (CNN) trained on the original MNIST dataset (see Methods), a classification accuracy of $\approx 96\%$ was achieved (confusion matrix in Fig. 4**f**), thereby validating the high-fidelity capture and reconstruction of complex stroke trajectories.

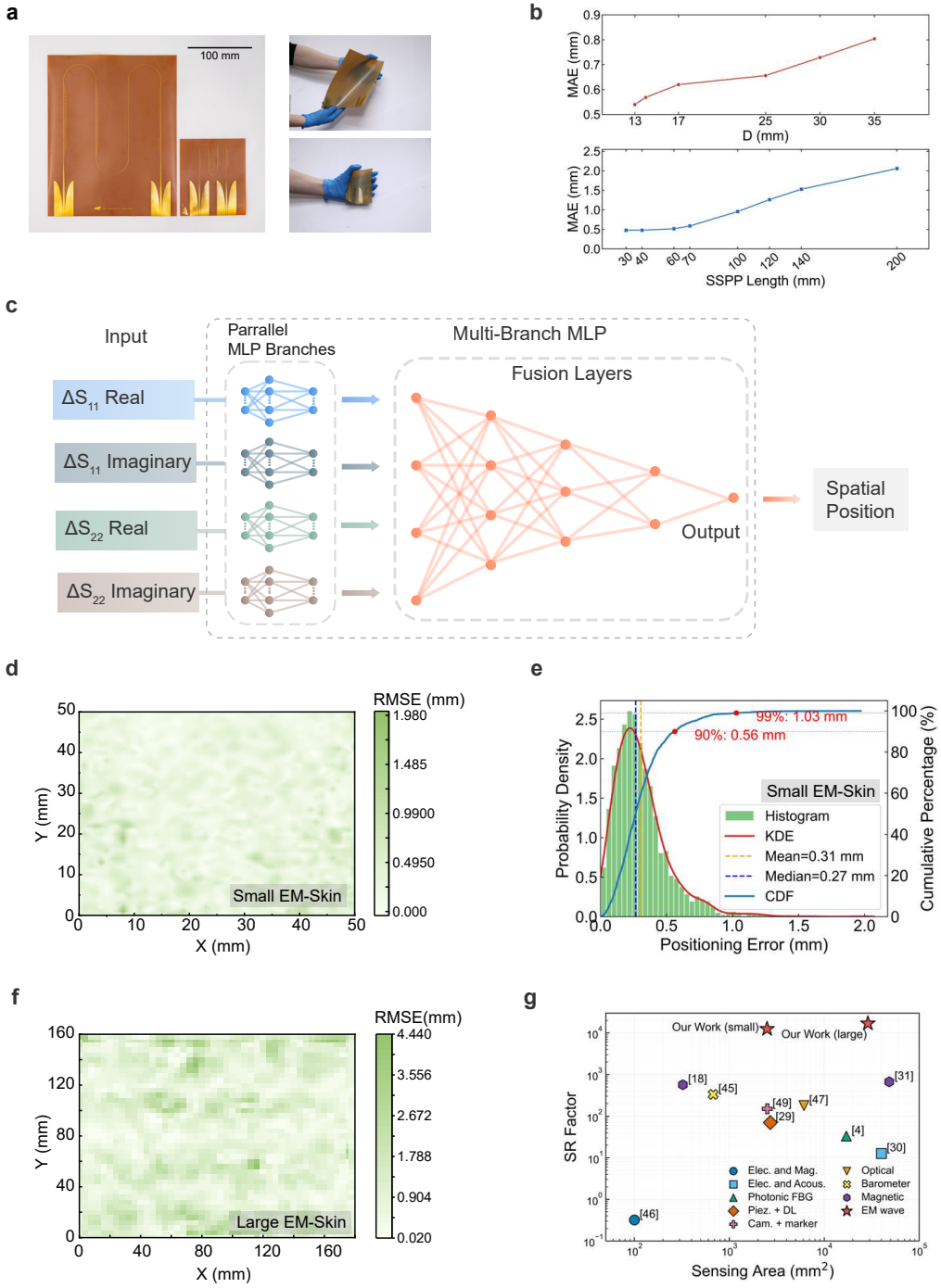

Fig. 3. Fabricated transmission lines and localization performance. a Photographs of the fabricated small and large transmission lines. Both devices are fabricated on a PI (polyimide) substrate, rendering them mechanically flexible. **b** Simulated mean *MAE* results as a function of line spacing between adjacent bending transmission lines and gap between SSPP lines shows sub-linear increase with dimension highlighting the scalability of this approach. **c** A multi-branch neural network is used to predict location from measured reflection coefficients. ΔS from both ports are separated into real and imaginary components, and processed by four small fully connected multi-layer perceptron (MLP) networks. Subsequently, these features are fused by a bigger MLP to yield the final spatial position. **d** Pixel-wise RMSE of localization error for the small transmission line exhibiting uniform coverage. **e** Cumulative distribution function (CDF) and kernel density estimation (KDE) of localization error for the small transmission line showing sub-mm mean and median localization errors. **f** Pixel-wise RMSE of localization error for the large transmission line. **g** Comparison of the SR factor as a function of sensing area between state-of-the-art super resolution e-skin works highlighting the superiority of our proposed EM-skin.

As a second example, a customized one-octave mini piano keyboard was implemented on the sensing surface, comprising seven diatonic notes and five accidentals (black keys). When a finger presses a key, the corresponding signature captured by the S-parameters enable identification of the pressed key with 100% accuracy even using a simple support vector machine (see Methods). Figure 4**g** and Supplementary Video 2 illustrate the application of the proposed EM-skin system as a piano, where it is used to play a popular song (Twinkle, Twinkle, Little Star).

Object recognition

Beyond localization, the EM-skin can also recognize different objects based on unique S-parameter signatures due to different material permittivities, shapes and sizes (Fig. 5**a**). Accordingly, eight sample objects of daily use (Fig. 5**c**, Supplementary Fig. S13) spanning metal, plastic, ceramic and composite materials were selected to create a dataset (Methods) of spectral signatures by placing the objects on the sensing plane. Using an XGBoost classifier (Supplementary Note S4 and Supplementary Note S5) due to limited dataset size, an overall recognition accuracy of 91.3% was achieved on this eight class recognition task. Further, visualizing the features of the XGBoost using t-SNE (Fig. 5**d**) showed distinct clusters for each object and a pronounced boundary between metallic and non-metallic objects. Motivated by this result, a binary classification task was further performed by grouping the objects into metallic versus non-metallic categories(Fig. S18). Under this setting, the XGBoost classifier achieves 100% accuracy, supporting the strong dielectric contrast between metals and non-metals, while also demonstrating that the proposed EM-skin system remains effective across diverse material classes.

Discussion

Scalable and high-precision e-skin is a long-standing goal in tactile sensing. However, enlarging the sensing area or spatial resolution typically leads to a rapid increase in the number of sensing nodes, wiring complexity, and cost making this goal challenging to achieve. Here, we demonstrated a flexible SSPP-based, single wire EM-skin system that can achieve sub-wavelength localization by using a multi-branch neural network to learn position-dependent features from frequency-swept S-parameter responses. By emulating the superimposing receptive fields mechanism of human skin and adopting a super-resolution strategy, tactile stimulus localization at one third of pixel size is achieved over EM-skins varying by one order of magnitude in area (from 5×5 to 16×18 cm^2). The mean SR factors exceed 10,000 substantially outperforming state-of-the-art solutions. The high localization accuracy indicates that the electromagnetic response of the SSPP transmission line is highly sensitive to local perturbations introduced by external objects. This sensitivity is mainly attributed to the strong field confinement of the SSPP structure, enabling high-precision human-computer interfaces. It also enables tiling of many EM-skin patches to cover whole robot bodies without significant interference. Further, the EM-skin is able to recognize different objects based on the spectral signature of their size, shape and permittivity. Achieving higher frame rates by using integrated circuits for spectrum sensing and measuring applied force by integrating a soft dielectric on the EM-skin are promising future directions of research. Overall, this work provides a new sensing modality for collaborative robots, where large area coverage of whole body is needed along with sensitive touch in the hands.

Methods

Spoof Surface Plasmon Polaritons Structure

Spoof surface plasmon polaritons (SSPPs) are engineered surface electromagnetic modes that replicate the behavior of natural surface plasmons at frequencies where metals act as perfect conductors. By patterning a metal surface with subwavelength periodic structures, SSPPs enable confined electromagnetic wave propagation from microwave to terahertz frequencies.

In the slow-wave regime, SSPPs support surface-wave propagation with strong electromagnetic confinement along the structured interface. This mode guides waves with low radiation loss and attenuation, limiting energy leakage and enabling efficient transmission along the surface. The combination of strong field confinement, low propagation loss and suppressed radiation makes SSPP structures well suited for flexible electromagnetic skins.

Along the guided SSPP path, impedance discontinuities and material inhomogeneities act as a continuous distribution of localized reflectors, and the total reflection measured at the input port is the coherent superposition of their individual contributions. Let s denote the propagation coordinate measured from the input port and $\rho(s)$ the local reflectivity per unit length. Under the weak-scattering approximation, the frequency-domain reflection coefficient is

$$\Gamma(\omega) \simeq \int_0^L \rho(s) \exp[-2j\beta(\omega)s]\, \mathrm{d}s, \tag{3}$$

where $\beta(\omega)$ is the frequency-dependent propagation constant of the guided mode, L is the total electrical length of the line, and the factor of two accounts for the round-trip phase accumulated by a wave that propagates to coordinate s and back. Equation (3)

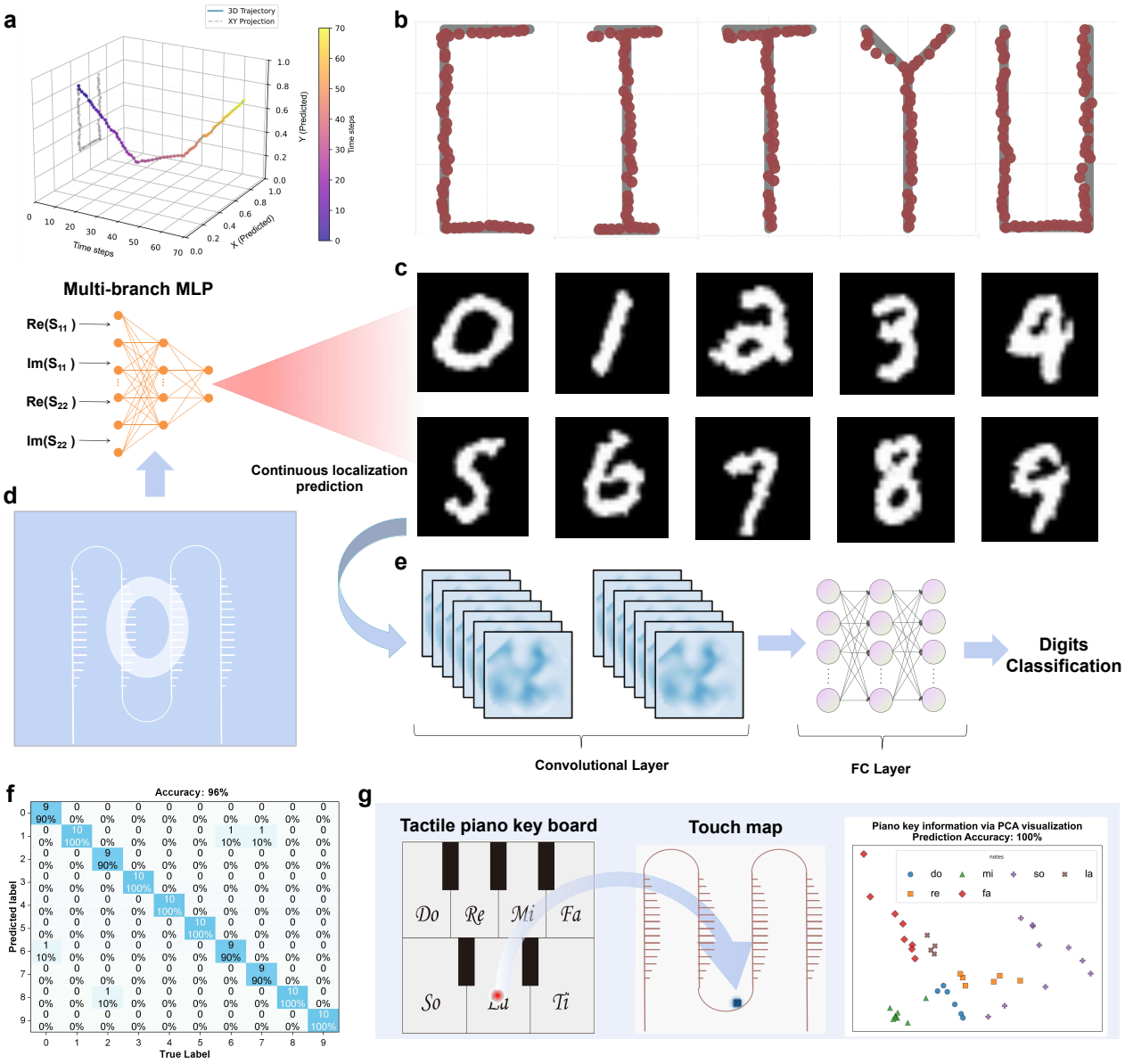

Fig. 4. Human–machine interaction applications. **a** Illustration of real-time trajectory recognition when an alphabet “C" is traced on the EM-skin by a robotic arm. **b** Trajectory recognition illustration for writing “CITYU" using single strokes. The gray region indicates the ground-truth trajectory, while the dark-red points show the recognized trajectory. **c** More complex characters with multiple strokes are written by the robotic arm following the contour of the digits 0-9 in the popular visual MNIST dataset. The interior is then filled to generate a localization-trajectory image compatible with MNIST-style inputs. **d** Illustration of a sample digit-shaped trajectory superimposed on the sensing plane of the EM-skin. **e** The MNIST-style trajectory images generated in (c) are fed into a CNN trained on the MNIST dataset to perform handwritten digit classification. **f** Confusion matrix for the handwritten digit classification task exhibiting overall accuracy $\approx 96\%$. **g** The EM-skin system was converted to a smart piano keyboard with seven musical notes and used to play the popular song “Twinkle, Twinkle, Little Star", as demonstrated in the supplementary video. The rightmost figure shows a PCA visualization of the input data corresponding to different notes during the performance.

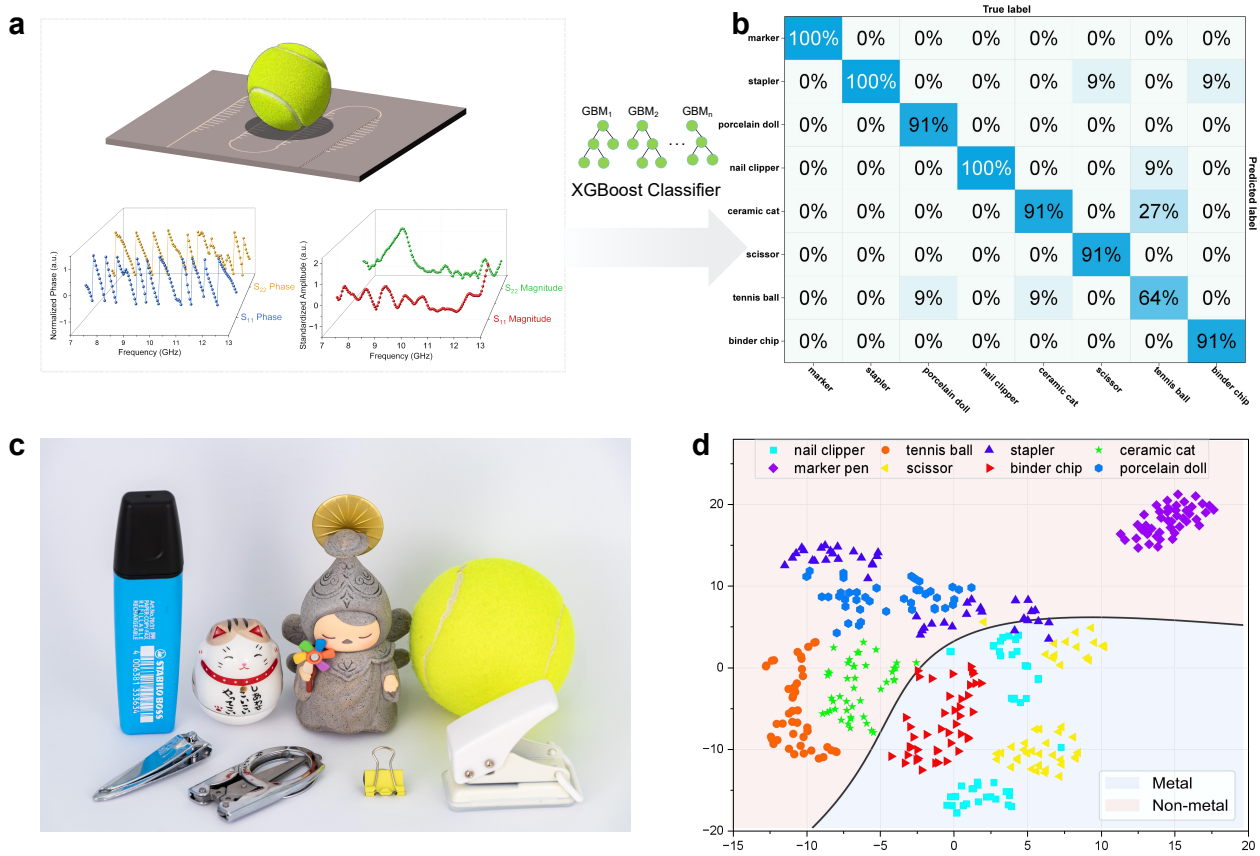

Fig. 5. Multi-material everyday object recognition. a Illustration of a sample object placed on the EM-skin and the corresponding high-dimensional reflection signals. A XG-boost classifier is used to distinguish different objects (shown in (c)). **b** Confusion matrix for the classification of the eight selected everyday objects with a resulting classification accuracy of $\approx 91.3\%$. **c** Photographs of the eight everyday objects used in this study made of different materials spanning metals, ceramics, plastic and composite materials. **d** T-SNE visualization of XGBoost leaf-index embeddings derived from the spectral reflection data. The reflection data shows clear clusters for each object and the space can also be divided into metallic and non-metallic regions, with the black solid line indicating the boundary.

provides a linear mapping from frequency-domain reflections to positions along the 1D propagation coordinate, but it localizes perturbations only along the line and cannot resolve objects in the surrounding plane.

To extend this concept to 2D sensing, the 1D transmission path is routed through an engineered planar topology, implemented here as a continuous meandering SSPP structure (Extended Data Fig. 1) parameterized by the SSPP length L_{spp} and the inter-segment distance D. This geometry maps the propagation coordinate s onto known positions (X,Y) in the sensing plane. Reflections are then no longer generated only by fixed impedance perturbations of the line; objects located outside the line yet within the near-field region also induce local perturbations through evanescent coupling to nearby segments, with a strength that decays with distance. The measured spectrum can therefore be interpreted as a geometry-weighted projection of the 2D perturbation distribution onto the 1D propagation path.

We discretize the sensing plane into N candidate points, with coordinates (x_p, y_p), object-induced response amplitudes q_p and area elements ΔA_p. The routed line is likewise divided into M segments, the mth of which is located at (X_m, Y_m) and carries a cumulative propagation coordinate s_m. Modeling the near-field coupling by a distance-decay weight $\exp(-\alpha\, d_{mp})$, where $d_{mp} = \sqrt{(x_p - X_m)^2 + (y_p - Y_m)^2}$ and $\alpha > 0$ is an effective decay constant, the effective reflection density induced at segment m is the superposition of contributions from all surface points,

$$r_m^{\text{eff}} = \sum_{p=1}^{N} q_p \exp(-\alpha\, d_{mp})\, \Delta A_p. \tag{4}$$

Substituting Eq. (4) into the discretized form of Eq. (3) and interchanging the finite sums separates the object response on the sensing plane from the phase accumulation along the routed path. Sampling the reflection spectrum at frequencies ω_ℓ, the forward model becomes

$$\Gamma_\ell \simeq \sum_{p=1}^{N} K_{\ell p}\, q_p, \qquad \Gamma \simeq \mathbf{K} q, \tag{5}$$

where Γ collects the measured reflection coefficients, q is the object-induced response distribution, and $\mathbf{K}$ is the geometry-dependent sensing matrix, with elements

$$K_{\ell p} = \Delta A_p \sum_{m=1}^{M} \exp\left[-\alpha \sqrt{(x_p - X_m)^2 + (y_p - Y_m)^2}\right] \exp[-2j\beta(\omega_\ell)\, s_m]\, \Delta s_m, \tag{6}$$

where Δs_m is the segment length. Each element of $\mathbf{K}$ thus combines the distance-dependent coupling from a surface point to all routed segments with the round-trip phase accumulated along the 1D path, and recovers the 1D limit of Eq. (3) when the coupling is confined to the line. A full step-by-step derivation, including the dual-port formulation, is given in Supplementary Section Supplementary Note S2.

Given a measured spectrum Γ and the calibrated sensing matrix $\mathbf{K}$, localization is formulated as the inverse problem of inferring the object position from the response distribution q that best explains the measured reflection. In our work this inverse mapping is not obtained by explicitly inverting $\mathbf{K}$, which omits practical non-idealities such as fabrication tolerances, frequency-dependent loss and port mismatch. Instead, $\mathbf{K}$ serves as a physical forward model, while the localization is learned directly from calibrated reflection spectra with a neural network.

2D SSPP E-skin Fabrication

We designed the two-dimensional transmission line based on the SSPP structure to achieve strong electromagnetic field confinement and efficient wave guidance at microwave frequencies. To provide two-dimensional area coverage, the transmission line was patterned into a serpentine configuration. The device was fabricated on a 0.11 mm-thick copper-clad polyimide substrate, selected for its flexibility and broadband dielectric stability. Copper patterns were directly structured onto the polyimide film via laser cutting. This method offers a low-cost, scalable fabrication approach, with estimated unit costs of approximately 10.6 USD for the small-scale design and 17 USD for the large-scale design.

We optimized the geometric parameters of the transmission line, including slot depth, period, and bend radii and using CST Studio Suite to maximize two-dimensional field coverage while minimizing reflection loss. Both simulation and experimental results in Fig. S4 and Fig. S5 confirmed that the return loss at both ports exceeded 10 dB across the operating bandwidth, ensuring adequate impedance matching and efficient power transmission.

Automated dataset acquisition for localization

We acquired the dataset using an automated data-acquisition system comprising a programmable motorized translation stage (8MT50 Motorized Translation Stages), a personal computer and a VNA (KEYSIGHT PNA-X Network Analyzer N5242B),

as shown in Extended Data Fig. 2. The computer sends control commands to both the VNA and the motorized stage. The motorized stage moves along the pre-defined trajectory, and the VNA records the S_{11} and S_{22} data after each movement is completed. The collected S_{11} and S_{22} data are subsequently processed on the PC.

The sensing area covered by the small EM-skin system is 50 mm $\times$ 50 mm. Because the electromagnetic field is distributed within the three-dimensional space above the transmission-line plane, we used a high-precision programmable motorized stage to control the probe and uniformly sample the entire three-dimensional space, enabling us to investigate the relationship between spatial coordinates and the S-parameters. The transmission-line plane is defined as the XY plane, and the Z axis is defined as the direction perpendicular to and above this plane. Along both the X and Y directions, the probe was moved with a step size of 1 mm. Along the Z direction, the probe was moved with a step size of 0.2 mm, over a sampling height ranging from 0 to 1 mm. In total, we obtained 13,005 samples, which were uniformly distributed within a three-dimensional volume of 50 mm $\times$ 50 mm $\times$ 1 mm. At each spatial position corresponding to one sample, the S_{11} and S_{22} data were measured by the VNA using a frequency-swept wave from 7 GHz to 13 GHz.

The sensing area covered by the large EM-skin system is 160 mm $\times$ 180 mm. To keep the time required for dataset construction within a practical range, we used a larger scanning step size of 4 mm along the X and Y directions. Along the Z direction, only two heights, z = 0 mm and z = 2.4 mm, were sampled to construct the dataset for the large transmission-line system. Therefore, the large-system dataset contains a total of 3,772 samples. In contrast to the small EM-skin system, the VNA measured the S_{11} and S_{22} data using a frequency-swept wave from 4 GHz to 10 GHz.

The data acquisition time of the system varies with the number of frequency sampling points and the acquisition bandwidth. For the small transmission line operating over a 6 GHz bandwidth with 121 frequency points, the mean acquisition time for a single dual-port measurement was 150 ms, with a maximum of 250 ms, corresponding to a minimum sampling rate of 4 Hz and a mean of approximately 6 Hz. There is an inherent trade-off between sampling rate and sensing accuracy: fewer frequency points accelerate acquisition but reduce the precision of sensing

Machine learning method for high-accuracy positioning

We adopted a multi-branch regression MLP architecture, which can be regarded as a variant of a conventional MLP. The rationale behind this design is based on physical intuition: each channel is expected to contain distinct features of the target object, while the data distributions across different channels may also vary. Therefore, instead of directly feeding all 121 data points from each of the four channels into a single MLP layer, we first employ four independent branch MLPs (Fully connected (FC) layer 121-160 for small and 120-576-288 for large one) as local feature extractors for the four input channels. The output features from the four branches are then concatenated and fed into a fusion MLP to perform global feature integration and two-dimensional coordinate prediction. To determine the optimal width and depth of each branch MLP and the fusion MLP, we employed a constrained neural architecture search strategy based on validation-set performance, as detailed in Section Supplementary Note S3. The final optimized network architectures for the small-scale EM-skin system (640-1024-640-512-384-256-160-2) and the large-scale EM-skin system (1152-1088-640-480-2), obtained after the neural architecture search procedure, can be found in Fig. S16 and Fig. S17, respectively.

The S-parameters obtained using the vector network analyzer (VNA) are complex-valued data. As reported in Ref.[38], reformatting the input signal plays a decisive role in enabling neural networks to more effectively learn features embedded in the data. Compared with directly using the magnitude and phase of the S-parameters as inputs, representing them in terms of their real and imaginary components produces smoother input curves and is therefore more favorable for training. In Fig. S8, we further evaluated the localization accuracy of neural networks with the same architecture under two different input representations. In terms of data preprocessing, for the magnitude, real-component, and imaginary-component inputs, we calculated the mean and variance of the data separately for each channel and then standardized the data channel by channel. For the phase signal, we normalized it to the range of $[-1, 1]$. The results clearly show that, for both the large-scale and small-scale sensing systems, neural networks using the real and imaginary components as inputs achieve better localization performance than those using magnitude and phase inputs. In Fig. S9 and Fig. S10, we also visualize the same set of data under the two representations. We attribute this difference to the abrupt phase discontinuity occurring around $\pm 180^\circ$, which may be highly unfavorable for neural network training.

For dataset splitting, in the larger-scale EM-skin system with 3772 sample points, we further evaluated the localization performance using 5-fold cross-validation. For each fold, ten different random seeds were used for training, and the final performance was represented by the averaged result. For the smaller-scale EM-skin system with 13005 sample points, we split the dataset into training, validation, and test sets at a ratio of 7 : 1.5 : 1.5. Five datasets were generated using five different random seeds for data splitting, and for each dataset, ten different random seeds were further used for model training. The final performance was then reported as the average over all runs.

During training, we used the Adam optimizer together with a learning-rate scheduler based on either ReduceLROnPlateau or CosineAnnealingLR. The mean squared error was used as the loss function. Considering the presence of environmental noise

during dataset acquisition, we mainly controlled the regularization strength by adding Gaussian noise to the input data and applying weight decay. An early-stopping strategy was also employed to prevent overfitting. The detailed training results for the larger-scale EM-skin system and the smaller-scale EM-skin system are presented in Extended Data Table 2 and Extended Data Table 3, respectively.

Investigation of localization accuracy limit

When acquiring training data using the automated dataset collection system for localization-model training, we found that a sampling pitch of 1 mm was already sufficient to achieve a localization RMSE below 1 mm. This observation naturally raises the question of whether further reducing the sampling pitch, for example to 0.5 mm, and thereby providing denser position labels together with more finely sampled S_{11} and S_{22} responses, could yield additional improvements in localization accuracy. In principle, such an improvement is plausible: S_{11} and S_{22} vary continuously with position, and a model with sufficient representational capacity should be able to exploit finer spatial labels, provided that the corresponding signal variations remain experimentally resolvable. In practice, however, VNA measurements are inevitably subject to noise, as well as additional instrumentation-induced uncertainties. Moreover, the effective bandwidth of the input signal determines the amount of position-dependent information encoded in S_{11} and S_{22}. These considerations suggest that localization performance is governed not simply by the spatial sampling pitch, but by the interplay between input bandwidth and the signal-to-noise ratio (SNR) of the position-induced variations, ΔS_{11} and ΔS_{22}, relative to measurement noise.

Extended Data Fig. 3**b–c** and Extended Data Fig. 4**b–c** shows that increasing the SNR consistently improves the SR factor and reduces the RMSE. As the measurement noise becomes negligible compared with the position-induced signal variations, the information encoded in ΔS_{11} and ΔS_{22} becomes more reliable, thereby enabling the model to learn a more discriminative mapping between the measured frequency responses and spatial position.

The effect of input bandwidth on regression performance is more complicated. For the small EM-skin, as shown in Extended Data Fig. 3**a**, increasing the bandwidth from 7 GHz to 11 GHz steadily reduces the localization error. However, further extending the upper frequency limit from 11 GHz to 13 GHz leads to a degradation in RMSE. This non-monotonic behavior reflects two competing effects. In the first regime, the performance gain arises because a broader bandwidth provides richer frequency-response information in S_{11} and S_{22}, thereby enhancing the discriminative power of the input features. In the second regime, however, as illustrated in Fig. 2**d**, the S_{11} and S_{22} responses in the 11–13 GHz range exhibit reduced spatial coverage across the sensing region and substantially stronger attenuation. This trend is also consistent with Fig. S10, where the signal magnitude in this frequency range is comparatively weak. Consequently, these spectral components become more susceptible to measurement noise; the resulting reduction in effective SNR outweighs the benefit of the additional bandwidth and ultimately leads to increased localization error. For the large EM-skin, as shown in Extended Data Fig. 4**a**, the localization error decreases continuously as the input bandwidth is increased from 4 to 8 GHz, which can likewise be attributed to the greater amount of position-dependent information captured over a broader frequency range. By contrast, extending the upper frequency limit from 8 to 10 GHz produces little further improvement in localization accuracy. This plateau suggests that, given the finite dataset size and model capacity, the predictive performance of the model has approached saturation as the input dimensionality increases. Moreover, the signals within the 8–10 GHz range undergo less attenuation than those at 11–13 GHz and therefore do not introduce low-signal-to-noise-ratio components that would otherwise degrade the localization performance.

Automated dataset acquisition for dynamic trajectory recognition

In the touchpad application of our proposed EM-skin, we recognized both relatively simple alphabetic trajectories and more complex MNIST-like digit patterns. To construct the dataset of alphabetic trajectories, we programmed a PC to control the motion trajectory of a robotic arm, which was used to draw the corresponding letter shapes. The motion trajectories of the robotic arm were generated by code, as shown by the gray background in Fig. 4**b**. The robotic arm moved with a step size of 1 mm, and the VNA rapidly sampled the S_{11} and S_{22} data whenever the robotic arm reached the corresponding position. Since different letters have different shapes, their corresponding trajectory lengths also varied. The trajectories corresponding to the letters in "CITYU" consisted of 55, 47, 42, 37, and 71 data points, respectively. The overall trajectory recognition process is illustrated in Fig. 4**a**.

When constructing the MNIST-like digit trajectories, the shapes were more complex and had a finite thickness, as indicated by the white regions in Fig. 4**c**. Since the motion trajectory of the robotic arm can only trace a single point at a time, we decomposed each MNIST-like digit into its inner and outer boundaries. Based on 100 different original MNIST images, we then generated 100 sets of robotic-arm trajectories using code, with each trajectory passing through both the inner and outer boundaries of the corresponding MNIST digit. The number of points in these trajectories ranged from 9 to 44. For the VNA data corresponding to each trajectory set, we subsequently recovered the trajectories using a regression-based localization model trained on the localization dataset, and reproduced the MNIST-like digits by filling the enclosed regions with color. More reconstructed MNIST-like digit results are shown in Fig. 4**f**.

CNN training for MNIST classification

To quantitatively evaluate the quality of the reconstructed MNIST-like digits, we trained a CNN based on the original MNIST dataset, and used our reconstructed MNIST-like digits, resized to the same 28×28 resolution, as the test set, as shown in Fig. 4**e**. The feature extractor contains two 3×3 convolutional layers with 32 channels, each followed by ReLU activation, and a 2×2 max-pooling layer that reduces the spatial resolution from 28×28 to 14×14. This is followed by a 3×3 convolution with 64 channels and another 2×2 max-pooling operation, producing 64 feature maps of size 7×7. The classification head flattens the features and applies a fully connected layer with 128 units and ReLU activation, followed by a final linear layer that outputs logits for 10 classes. The model achieves a final classification accuracy of 96%, and the corresponding confusion matrix is shown in Fig. 4**f**.

Dataset acquisition for object classification and smart mini piano keyboard

For the object classification application, the most common objects are selected as shown in Fig. S6. To collect the data, each object is placed on the transmission line at 56 different positions, and the VNA captures the corresponding scattering parameters. The acquired data are then divided into training and testing sets. A dot grid is printed on the surface to ensure that different objects can be placed at identical locations, so that the data variation is caused solely by the difference between objects.

For the piano application, as shown in Fig. S7, a printed piano board is placed on the transmission line with seven notes spanning one octave. The system is configured to capture data at 1-second intervals, during which the finger moves between notes. For each note, the finger is placed at different positions within the corresponding area, and 100 measurements are collected for training. The finger then plays a song, and the trained model reconstructs the melody in real time.

Machine learning method for object classification and smart mini piano keyboard

For object classification, we employed an XGBoost-based classifier to classify daily objects made of eight different materials. Since each class contains only 56 data samples, compact and lightweight machine-learning algorithms are more suitable than neural networks for such small-sample learning tasks. Regarding dataset splitting, we randomly divided the 56 samples of each object into training and test sets with a 4:1 ratio, ensuring that the proportions of each object category remain approximately consistent in both the training and test sets. As shown in Fig. S12, we compared the performance of four machine-learning classification algorithms suitable for small-sample learning, namely Logistic Regression based classifier, L1 Logistic Regression based classifier, Linear SVM based classifier, and XGBoost based classifier, on our object-classification dataset. The results clearly show that XGBoost achieves the highest classification accuracy. Subsequently, we further performed a grid search to find the optimal hyperparameter configuration for XGBoost. Another reason for selecting XGBoost is its good interpretability. We further aimed to use XGBoost as a feature extractor to investigate the relationship between S-parameters and object materials. As shown in Fig. 5**d**, the XGBoost-based feature extractor identifies a boundary between metallic and non-metallic materials. This finding is consistent with our theoretical expectation, indicating that XGBoost also serves as an effective feature extractor in this task. The detailed analysis of the classification errors is provided in Supplementary Note S5.

In the application of the smart mini piano keyboard, the training set, test set, and the additional test set used for playing "Twinkle, Twinkle, Little Star" were all collected through independent experiments. The detailed data-acquisition process is described in previous section. Our training set contains 1,200 samples corresponding to 7 piano keys. In addition, the test set is balanced, with 14 samples per class. In the additional test set for "Twinkle, Twinkle, Little Star," there are 42 test samples, corresponding to the 42 notes in the piece. Ultimately, across training, testing, and additional test set, even the simplest SVM can achieve 100% accuracy in recognizing the seven keys.

Data availability

The data that support the findings of this study are available from the corresponding author upon reasonable request.

Code availability

All the custom codes deemed central to the conclusions are available from the corresponding authors upon reasonable request.

Acknowledgments

This work was supported in part by CityU 11212823; in part by CityU 21207824.

Author contributions statement

A. B and G. W conceived the idea and supervised the project jointly. G. L, J. D and Y. S performed experiments jointly. J. D performed electromagnetic simulations. G. L performed machine learning experiments. G. L and J. D wrote the manuscript with inputs from all authors.

Ethics declaration

Not applicable.

Competing interests

The authors declare no competing interests.

References

1. Sankar, S. *et al.* A natural biomimetic prosthetic hand with neuromorphic tactile sensing for precise and compliant grasping. *Sci. Adv.* **11**, eadr9300, DOI: 10.1126/sciadv.adr9300 (2025).
2. Mao, Q., Liao, Z., Yuan, J. & Zhu, R. Multimodal tactile sensing fused with vision for dexterous robotic housekeeping. *Nat. Commun.* **15**, 6871 (2024).
3. Li, G., Liu, S., Wang, L. & Zhu, R. Skin-inspired quadruple tactile sensors integrated on a robot hand enable object recognition. *Sci. Robotics* **5**, eabc8134 (2020). https://www.science.org/doi/pdf/10.1126/scirobotics.abc8134.
4. Massari, L. *et al.* Functional mimicry of Ruffini receptors with fibre Bragg gratings and deep neural networks enables a bio-inspired large-area tactile-sensitive skin. *Nat. Mach. Intell.* **4**, 425–435, DOI: 10.1038/s42256-022-00487-3 (2022).
5. Zhang, N. *et al.* Soft robotic hand with tactile palm-finger coordination. *Nat. Commun.* **16**, 2395 (2025).
6. Liu, Z. *et al.* A three-dimensionally architected electronic skin mimicking human mechanosensation. *Science* **384**, 987–994 (2024).
7. Sundaram, S. *et al.* Learning the signatures of the human grasp using a scalable tactile glove. *Nature* **569**, 698–702, DOI: 10.1038/s41586-019-1234-z (2019).
8. Hong, W. *et al.* Self-adaptive cardiac optogenetics device based on negative stretching-resistive strain sensor. *Sci. Adv.* **7**, eabj4273 (2021).
9. Gong, S. *et al.* Hierarchically resistive skins as specific and multimetric on-throat wearable biosensors. *Nat. Nanotechnol.* **18**, 889–897 (2023).
10. Chen, Y. *et al.* Capacitive in-sensor tactile computing. *Nat. Commun.* **16**, DOI: 10.1038/s41467-025-60703-7 (2025).
11. Boutry, C. M. *et al.* A hierarchically patterned, bioinspired e-skin able to detect the direction of applied pressure for robotics. *Sci. Robotics* **3**, eaau6914 (2018).
12. Wang, T., Zhao, Y. & Wang, Q. A flexible iontronic capacitive sensing array for hand gesture recognition using deep convolutional neural networks. *Soft Robotics* **10**, 443–453 (2023).
13. Sun, K. *et al.* Growth of ultralong zno microwire and its application in isolatable and flexible piezoelectric strain sensor. *physica status solidi (a)* **207**, 488–492, DOI: https://doi.org/10.1002/pssa.200925468 (2010). https://onlinelibrary.wiley.com/doi/pdf/10.1002/pssa.200925468.
14. Tang, Y. *et al.* Digital channel–enabled distributed force decoding via small datasets for hand-centric interactions. *Sci. Adv.* **11**, eadt2641 (2025).
15. Funk, N., Helmut, E., Chalvatzaki, G., Calandra, R. & Peters, J. Evetac: An event-based optical tactile sensor for robotic manipulation. *IEEE Transactions on Robotics* **40**, 3812–3832 (2024).
16. Chen, L. *et al.* Spike timing–based coding in neuromimetic tactile system enables dynamic object classification. *Science* **384**, 660–665, DOI: 10.1126/science.adf3708 (2024).
17. Li, N. *et al.* A triboelectric-inductive hybrid tactile sensor for highly accurate object recognition. *Nano Energy* **96**, 107063 (2022).
18. Makushko, P. *et al.* Scalable magnetoreceptive e-skin for energy-efficient high-resolution interaction towards undisturbed extended reality. *Nat. Commun.* **16**, 1647 (2025).

19. Yan, Y. *et al.* Soft magnetic skin for super-resolution tactile sensing with force self-decoupling. *Sci. Robotics* **6**, eabc8801, DOI: 10.1126/scirobotics.abc8801 (2021).

20. Makushko, P. *et al.* Scalable magnetoreceptive e-skin for energy-efficient high-resolution interaction towards undisturbed extended reality. *Nat. Commun.* **16**, 1647, DOI: 10.1038/s41467-025-56805-x (2025).

21. Hellebrekers, T. *et al.* Soft Magnetic Tactile Skin for Continuous Force and Location Estimation Using Neural Networks. *IEEE Robotics Autom. Lett.* **5**, 3892–3898, DOI: 10.1109/lra.2020.2983707 (2020).

22. Wang, C. *et al.* Tactile sensing technology in bionic skin: A review. *Biosens. Bioelectron.* **220**, 114882 (2023).

23. Qu, J. *et al.* Recent Progress in Advanced Tactile Sensing Technologies for Soft Grippers. *Adv. Funct. Mater.* (2023).

24. Dahiya, R. S., Mittendorfer, P., Valle, M., Cheng, G. & Lumelsky, V. J. Directions toward effective utilization of tactile skin: A review. *IEEE Sensors J.* **13**, 4121–4138 (2013).

25. Bitonneau, D. *et al.* Design of an industrial human-robot system through participative simulations—tank cleaning case study. In *2017 IEEE/SICE International Symposium on System Integration (SII)*, 421–428, DOI: 10.1109/SII.2017.8279363 (2017).

26. Johansson, R. & Flanagan, J. 6.05-tactile sensory control of object manipulation in humans. *Senses Compr. Ref. Acad. Press. NY NY* **67**, 86 (2008).

27. Abraira, V. E. & Ginty, D. D. The sensory neurons of touch. *neuron* **79**, 618–639 (2013).

28. Handler, A. & Ginty, D. D. The mechanosensory neurons of touch and their mechanisms of activation. *Nat. Rev. Neurosci.* **22**, 521–537 (2021).

29. Harvey, M. A., Saal, H. P., Dammann III, J. F. & Bensmaia, S. J. Multiplexing stimulus information through rate and temporal codes in primate somatosensory cortex. *PLoS biology* **11**, e1001558 (2013).

30. Kong, D. *et al.* Super-resolution tactile sensor arrays with sparse units enabled by deep learning. *Sci. AdvAnceS* (2025).

31. Park, K. *et al.* A biomimetic elastomeric robot skin using electrical impedance and acoustic tomography for tactile sensing. *Sci. Robotics* **7**, DOI: 10.1126/scirobotics.abm7187 (2022).

32. Hu, H. *et al.* Large-area magnetic skin for multi-point and multi-scale tactile sensing with super-resolution. *npj Flex. Electron.* **8**, DOI: 10.1038/s41528-024-00325-z (2024).

33. Lepora, N. F. & Ward-Cherrier, B. Superresolution with an optical tactile sensor. In *2015 IEEE/RSJ International Conference on Intelligent Robots and Systems (IROS)*, 2686–2691, DOI: 10.1109/IROS.2015.7353744 (IEEE, Hamburg, Germany, 2015).

34. Gao, Z., Wu, L., Gao, F., Luo, Y. & Zhang, B. Spoof plasmonics: from metamaterial concept to topological description. *Adv. Mater.* **30**, 1706683 (2018).

35. Liu, X. *et al.* Planar surface plasmonic waveguide devices based on symmetric corrugated thin film structures. *Opt. Express* **22**, 20107–20116 (2014).

36. Ye, L. *et al.* Strongly confined spoof surface plasmon polaritons waveguiding enabled by planar staggered plasmonic waveguides. **6**, 38528.

37. Tang, W. X., Zhang, H. C., Liu, J. F., Xu, J. & Cui, T. J. Reduction of radiation loss at small-radius bend using spoof surface plasmon polariton transmission line. **7**, 41077.

38. Qian, C., Kaminer, I. & Chen, H. A guidance to intelligent metamaterials and metamaterials intelligence. *Nat. Commun.* **16**, 1154 (2025).

39. Fromenteze, T. *et al.* Computational polarimetric microwave imaging. *Opt. Express* **25**, 27488–27505 (2017).

40. Hunt, J. *et al.* Metamaterial apertures for computational imaging. *Science* **339**, 310–313 (2013).

41. Jiang, P., Wang, T., Liu, L. & Luo, G. Q. High scanning-rate leaky-wave antenna for frequency-diverse microwave imaging. *IEEE Antennas Wirel. Propag. Lett.* 1–5 (2025).

42. Liu, B., Wu, J., Zhang, Q. & Wong, H. High-speed wide-angle sensing and imaging by WideBand metasurfaces with joint frequency, polarization, and spatial diversities. *Laser Photonics Rev.* **18**, 2400207 (2024).

43. Liu, B., Zhang, Q. & Wong, H. Multifunctional reconfigurable intelligent surface for wideband beamforming and frequency-and-spatial-diverse microwave sensing. *IEEE Trans. Antennas Propag.* **73**, 1135–1148 (2025).

44. Xiao, S. *et al.* Demonstration of multitarget wireless sensing using high-scanning-rate coupled-patch antenna. *IEEE Antennas Wirel. Propag. Lett.* **23**, 3406–3410 (2024).

45. Zhao, M. *et al.* Frequency-diverse bunching metasurface antenna for microwave computational imaging. *IEEE Trans. Antennas Propag.* **72**, 3950–3961 (2024).

46. Sun, H. & Martius, G. Guiding the design of superresolution tactile skins with taxel value isolines theory. *Sci. Robotics* **7**, DOI: 10.1126/scirobotics.abm0608 (2022).

47. Ge, J. *et al.* A bimodal soft electronic skin for tactile and touchless interaction in real time. *Nat. Commun.* **10**, 4405, DOI: 10.1038/s41467-019-12303-5 (2019).

48. Piacenza, P., Behrman, K., Schifferer, B., Kymissis, I. & Ciocarlie, M. A sensorized multicurved robot finger with data-driven touch sensing via overlapping light signals. *IEEE/ASME Transactions on Mechatronics* **25**, 2416–2427, DOI: 10.1109/TMECH.2020.2975578 (2020).

49. LeCun, Y., Cortes, C. & Burges, C. J. The mnist database of handwritten digits. (1998).

50. Lepora, N. F. & Ward-Cherrier, B. Superresolution with an optical tactile sensor. In *2015 IEEE/RSJ International Conference on Intelligent Robots and Systems (IROS)*, 2686–2691, DOI: 10.1109/IROS.2015.7353744 (2015).

Extended Data

492

Extended Data Table 1 | A comparison between our work and state-of-the-art tactile sensors based on SR technology.

Sensor name	Transduction method	Sensing area (mm^2)	No. of used sensors	Wire complexity	Localization RMSE (mm)	Avg. SR factor
Ge et al.[47]	Electrical	100	4	4N	5	0.32
Park et al.[31]	Electrical and acoustic	40000	57	0	4.2	12.66
Luca Massari et al.[4]	Photonic fibre Bragg	17082	16	1	3.2 (median)	33.187
Depeng Kong et al.[30]	Piezoresistive + deep learning	2700	23	2N	0.73	70.12
TacTip[50]	Camera + marker	2513	532	##	0.1 (MAE)	∼150
Piacenza et al.[48]	Optical	∼6107	30	##	0.6	∼180
Sun et al.[46]	Barometer	676	25	N	0.16	334
Yan et al.[19]	Magnetic	324	9	0	0.142	568.3
Hao Hu et al.[32]	Magnetic	48400	16	0	1.2	668.67
Our work (small)	Electromagnetic wave	2500	1	1	0.368	**12477.4**
Our work (large)	Electromagnetic wave	28800	1	1	1.209	**16886.4**

Notes. "Wire complexity" refers to the number of signal lines required to read out signals from the sensors. "##" indicates that the wire complexity was not specified in the original work. "∼" denotes an approximate value. The SR factor is calculated as

$$\text{SR factor} = \frac{\text{Area}}{n\pi \text{RMSE}_x \text{RMSE}_y},$$

where n denotes the number of sensing elements used for localization[46].

Extended Data Table 2 | Detailed neural-network localization results for the large EM-skin under five-fold cross-validation.

Fold	RMSE_x (mm)	RMSE_y (mm)	SR factor	RMSE_{xy} (mm)
1	0.6708	1.1164	13145.933	1.3127
2	0.4756	1.0414	18619.479	1.1455
3	0.4635	1.1284	17654.612	1.2208
4	0.4889	1.1035	17114.392	1.2075
5	0.4955	1.0492	17897.878	1.1620
Mean	**0.5188**	**1.0878**	**16886.459**	**1.2097**

RMSE_x and RMSE_y denote the root-mean-square localization errors along the x and y directions, respectively. RMSE_{xy} denotes the two-dimensional localization error. SR, super-resolution.

Extended Data Table 3 | Detailed neural-network localization results for the small EM-skin.

Run	Mean RMSE$_x$ (mm)	Mean RMSE$_y$ (mm)	Mean RMSE$_{xy}$ (mm)	Mean SR factor
1	0.281997	0.247784	0.375514	11947.939890
2	0.276980	0.241043	0.367333	12962.732236
3	0.268010	0.229562	0.353070	13419.273524
4	0.285187	0.237676	0.371337	12024.018201
5	0.280737	0.242905	0.371402	12032.915594
Mean	**0.278582**	**0.239794**	**0.367731**	**12477.375889**

RMSE$_x$ and RMSE$_y$ denote the root-mean-square localization errors along the x and y directions, respectively. RMSE$_{xy}$ denotes the two-dimensional localization error. The reported values are averaged over repeated neural-network training runs. SR, super-resolution.

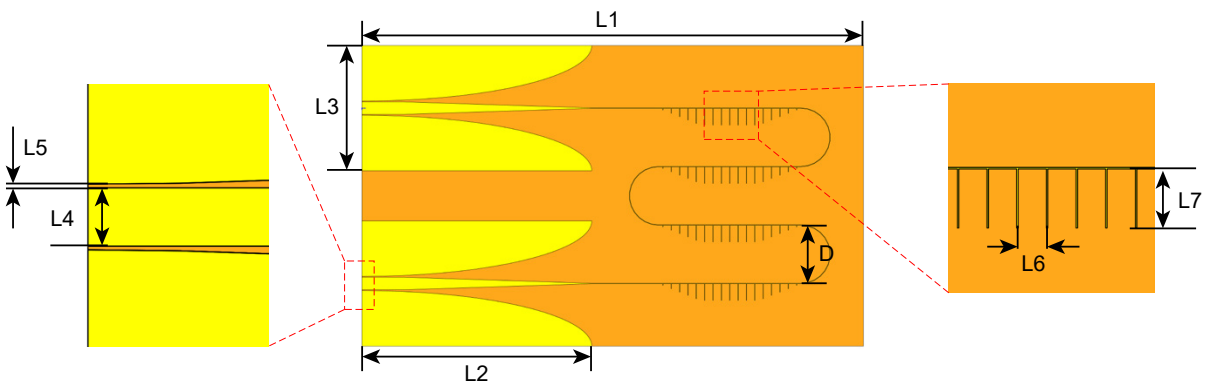

Extended Data Fig. 1 | Design and dimensions of the SSPP transmission line.

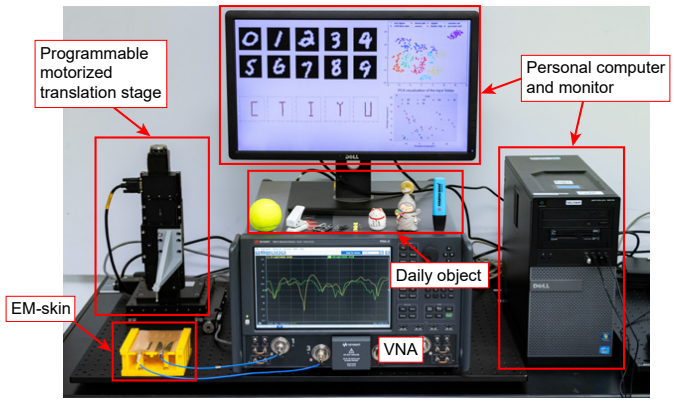

Extended Data Fig. 2 | Test environment setup with a VNA, a computer and a motor.

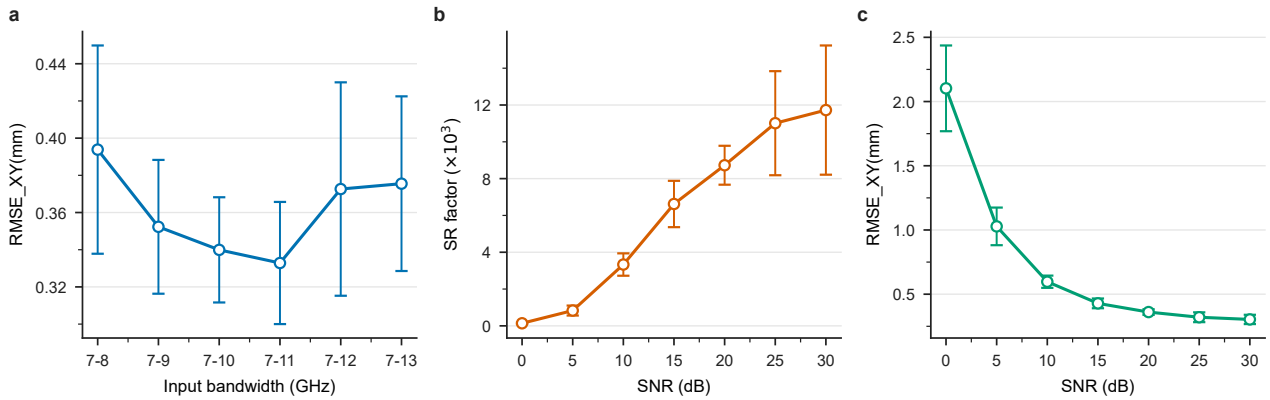

Extended Data Fig. 3 | Simulation results of localization error (RMSE) and SR factor for the small EM-skin under different SNRs and input signal bandwidths.

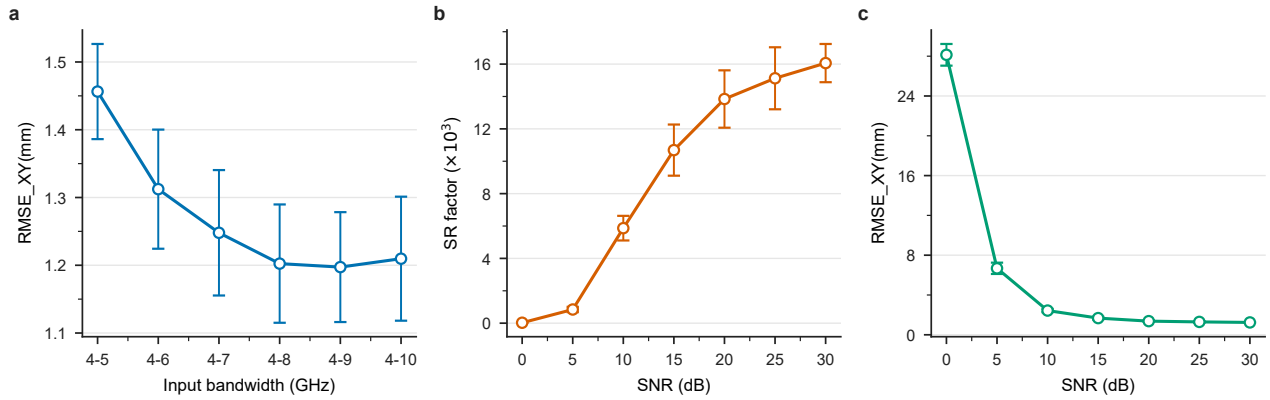

Extended Data Fig. 4 | Simulation results of localization error (RMSE) and SR factor for the large EM-skin under different SNRs and input signal bandwidths.

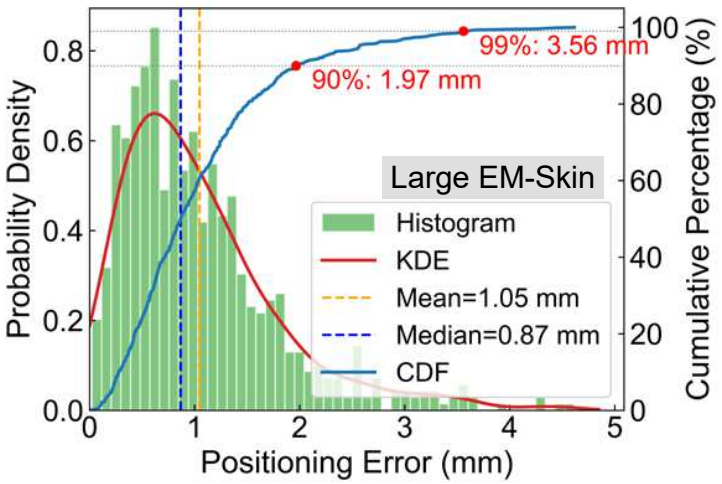

Extended Data Fig. 5 | Cumulative distribution function of the localization error for the large EM-skin.

Supplementary Files

This is a list of supplementary files associated with this preprint. Click to download.

- SIGuide.doc
- SupplementaryInformation.pdf
- SupplementaryVideo2PianoKeyInteractionDemonstration.mp4
- SupplementaryVideo1RoboticWritingTrajectoryReconstruction.mp4